Journal of Magnetic Resonance 368 (2024) 107782

Contents lists available at ScienceDirect

Journal of Magnetic Resonance

journal homepage: www.elsevier.com/locate/jmr

Simultaneous multinuclear MRI via a single RF channel

Mohammad Rasool Vaezi K., Jan G. Korvink *, Mazin Jouda *

Karlsruhe Institute of Technology (KIT), Institute of Microstructure Technology, Karlsruhe 76131, Germany

ARTICLE INFO

Keywords:
Parallel multi-nuclear MRI
Digital lock-in amplifier
Single RF-channel MRI
Broadband RF coil

ABSTRACT

Magnetic resonance imaging (MRI) stands as one of the most powerful noninvasive and non-destructive imaging techniques, finding extensive utility in medical and industrial applications. Its ability to acquire signals from multiple nuclei grants it additional levels of strength by providing multi-dimensional datasets of the object under test. However, this typically requires dedicated hardware to detect each nucleus. In this paper, we report on the use of a digital lock-in amplifier to perform simultaneous multi-nuclear MRI with a single physical radio frequency (RF) channel. While we showcase this concept by demonstrating the results of fully parallel (TX and RX) ^{1}H and ^{19}F MRI images, we emphasize that it is not limited to two nuclei but can accommodate more nuclei with no extra cost on the hardware or scan time. The scalability is virtually unlimited, constrained only by the processing speed of the digital unit. Furthermore, we demonstrate that the quality of parallel imaging with SNR of 54 is comparable to the commercial single channel with SNR of 43. Thus with no reduction in imaging quality, the proposed concept promises a tremendous reduction in scan time, system complexity, and hardware costs.

1. Introduction

Magnetic resonance imaging (MRI) is one of the most powerful non-invasive and non-destructive imaging techniques available today. While MRI's major applications are medical including brain imaging [1,2], cardiovascular imaging [3], and neurosciences [4], it is also exploited in non-medical applications including plant imaging [5] and monitoring mass transport in porous media [6]. While the vast majority of MRI applications rely on the acquisition of nuclear magnetic resonance (NMR) signals from the ^{1}H spins, multinuclear MRI, in which the NMR signals from other nuclei existing in the sample are acquired, emerges as a powerful tool that can provide complementary multi-dimensional information on the sample [7]. For instance, the acquisition of the NMR signals of ^{31}P can help to study the metabolites in the liver [8], while the hyperpolarized Xenon (^{129}Xe) is particularly useful for functional lung imaging [9]. On the other hand, ^{19}F MRI proved valuable for monitoring the uptake and distribution maps of fluorinated molecules in plants [10]. Multinuclear MRI usually demands specialized RF transceiver channels for each nucleus due to their varying frequencies. This need is especially pronounced when simultaneous acquisition is required. In several scenarios, simultaneous multinuclear MRI is essential for shortening scan time, capturing temporally and spatially correlated data across different nuclei, and comparing multinuclear data under identical transient stimuli.

Numerous efforts have been undertaken to enhance the hardware and RF circuitry to facilitate multi-nuclear MRI. For instance, Keupp et al. [11] reported on the use of a double-resonance RF coil, tuned to the frequencies of ^{19}F (120 MHz) and ^{1}H (128 MHz), for parallel MRI applications. This involved the use of two RF digital synthesizers for excitation and two receivers for simultaneous acquisition. The timing and gradient fields were configured for ^{19}F gradient-echo imaging, requiring a 6% rescaling of the ^{1}H images to account for the disparity in gyromagnetic ratios. Following up on this concept, Keupp et al. [12] broadened its application to encompass the employment of the simultaneously acquired ^{1}H and ^{19}F datasets to perform motion correction on the ^{19}F imaging agents and consequently achieve enhanced quantification. An additional illustration showcasing the advantages of parallel MRI in acquiring structurally correlated ^{1}H and metabolic ^{13}C images, both spatially and temporally, was highlighted by Gordon et al. [13]. Using a double-resonance ^{1}H/^{13}C coil and two RF channels, they demonstrated the utilization of motion information obtained from the ^{1}H data to mitigate motion artifacts in dynamic metabolic measurements. Multinuclear acquisition is also appealing for NMR spectroscopy [14]. In 2006, Kupce and colleagues [15] introduced PANSY (parallel acquisition NMR spectroscopy), demonstrating how the parallel acquisition of multinuclear NMR signals with multiple receivers can significantly reduce the experiment time in multi-dimensional NMR spectroscopy. In 2007, Kupce et al. [16] reported the simultaneous recording of two-dimensional NMR spectra correlating both ^{1}H and ^{19}F nuclei with either ^{13}C or ^{15}N using two receiver channels corresponding to the ^{1}H and ^{19}F nuclei.

* Corresponding authors.
E-mail addresses: jan.korvink@kit.edu (J.G. Korvink), mazin.jouda@kit.edu (M. Jouda).

https://doi.org/10.1016/j.jmr.2024.107782
Received 12 May 2024; Received in revised form 26 September 2024; Accepted 30 September 2024
Available online 9 October 2024

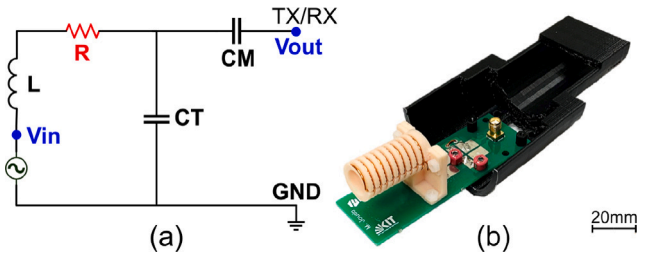

Fig. 1. (a) Schematic diagram of the tuning and matching circuit used. V_{in} represents the detected NMR signal during the reception phase. (b) The manufactured solenoidal BB-Coil mounted on a 3D-printed support to facilitate attaching it to the MRI probe. The external resistor, R, that is used to increase the bandwidth of the resonator is indicated in red.

In this paper, we introduce a technique for acquiring multiple nuclear MR images using a single radiofrequency channel. To validate this approach, we showcase its application in a parallel experiment involving both ^{1}H and ^{19}F MR imaging. Furthermore, we illustrate that this method, employing digital lock-in demodulation, can be expanded to encompass up to eight nuclei utilizing the same RF channel.

2. Methods

2.1. Coil design

Coil manufacturing for multinuclear MRI is a specialized field that involves crafting sophisticated RF coils to unlock the potential of diverse nuclei for advanced imaging and spectroscopy. The primary objective of this paper is to design a unified (single) RF channel and coil, centralizing the focus on advancing coil manufacturing for multinuclear MRI. ^{1}H and ^{19}F nuclei, resonating at approximately 45 MHz and 42 MHz, respectively, have been employed to demonstrate the experiment within a commercial 1.05 T magnet (ICON preclinical MRI scanner, Bruker Biospin, Ettlingen). With a 3 MHz frequency gap, we face a choice between two approaches: either developing a double resonance coil or engineering a single resonance broad-band (BB) coil to cover both frequencies. To accommodate this requirement, a solenoid coil in series with a resistor was designed beside a simple tuning and matching topology Fig. 1. The coil was made of a copper wire wound around a resin-based 3D-printed support. Advanced Design System (ADS) software from Keysight was utilized to determine and optimize the capacitors required for the circuit to resonate at 43.075 MHz frequency. Through this approach, the broadband coil effectively encompasses both proton and fluorine resonances, eliminating the necessity for constructing a double resonant topology. This decision is motivated by two factors: the proximity of proton and fluorine precession frequencies, and the potential complexity associated with the increased number of trimmer capacitors required for tuning and matching in a double resonance coil. The added resistor caused the Q-factor of the coil to drop from 172 to 18. Further information on the S_{11} reflection curve of the coil and the impact of the added resistor on the coil's sensitivity is available in the supplementary material. It is worth noting that the primary focus of the paper is to demonstrate the feasibility and potential of using a single digital RF channel to perform simultaneous multinuclear MRI with the full potential of expanding the number of nuclei at no extra cost in hardware, image quality, or system complexity.

2.2. Lock-in amplifier

Digital lock-in amplifiers digitize signals at high rates, conducting all subsequent signal-processing tasks in the digital domain. They present distinct features, including elevated precision attained through the application of advanced digital processing algorithms, frequency agility where fast switching between different frequencies is readily possible, and flexibility enabled by the rapid adjustment of processing parameters. Earlier studies by our group demonstrated the effectiveness of these amplifiers in dynamically adjusting the receiver gain during an NMR experiment to make optimal use of the receiver's analog-to-digital converter (ADC) dynamic range [17]. Additionally, they showcased the amplifiers functioning as a secondary RF channel in a commercial NMR environment [18].

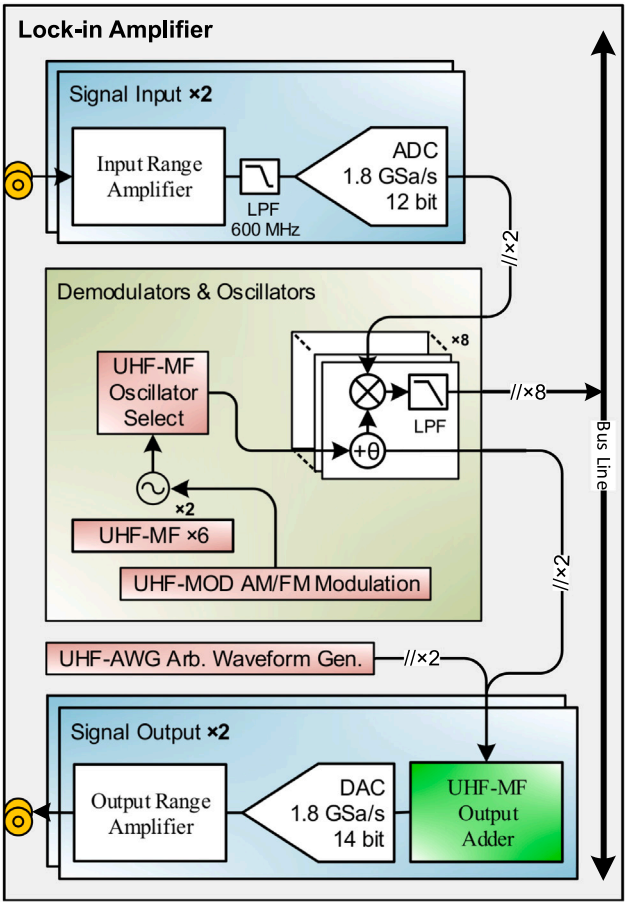

Fig. 2. A block diagram highlighting the various modules of the UHFLI and illustrating their interconnections and interactions.

This paper benefits from the advantages of the UHFLI (ultra-high-frequency lock-in) digital lock-in amplifier (Zurich Instruments) coupled with digital coding to run parallel multinuclear excitation and acquisition with a single channel. As depicted in Fig. 2, the key components of the UHFLI include two RF input channels digitizing input signals with a 12 bits vertical resolution at a fixed sample rate of 1.8 GSa/s, eight demodulators which can be dynamically and independently configured in terms of demodulation frequency and bandwidth, two arbitrary waveform generators (AWGs) connected to two RF modulators, and two RF output channels running at 1.8 GSa/s with 14-bit resolution. As is detailed in the following sections, a single or both RF output channels can be used to excite multiple nuclei, while a single RF input channel can be employed to acquire a frequency multiplexed free induction decay carrying the information of multiple nuclei. This combined signal is subsequently separated using digital demodulators equipped with low-pass filters (LPF), capable of accurately isolating each nucleus's specific bandwidth.

2.3. Experiment diagram

Fig. 3 illustrates the experimental diagram demonstrating the interface between the UHFLI and the Bruker system. Two schemes for

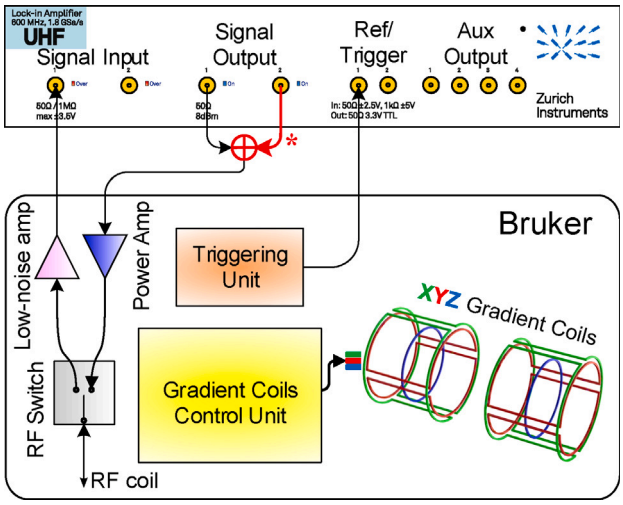

Fig. 3. A connection diagram demonstrating the interface between the Bruker system and the digital lock-in amplifier (UHFLI). The red connection, marked with an asterisk, illustrates the alternative hardware-efficient RF excitation scheme that is detailed in Section 3.2.

RF excitation are considered in this paper. In the first, the output RF channels are added using an RF combiner (Z99SC-62-S+, Mini-Circuits) and then connected to the Bruker 200 W power amplifier (PA), whereas in the second scheme, a single RF output channel is employed to carry out the multinuclear excitation. In the reception phase, a single RF input channel receives the amplified signal from the low-noise amplifier (LNA). Here we used the Bruker LNA which exhibits a noise figure of 0.8 dB. Additionally, the internal RF switch of the Bruker system was used to manage the transition between the excitation and acquisition phases of the MRI sequence. The use of a Bruker analog frontend (LNA, PA, and RF switch) was selected for its high performance and to ensure an accurate comparison between the UHFLI and Bruker transceivers. To maintain synchronization and timing precision, a triggering unit initiates the lock-in amplifier's operation through a programmable TTL signal. Furthermore, for obtaining three-dimensional multinuclear MRI, the system utilizes the XYZ gradient coil control unit driven by the Bruker system.

2.4. The pulse sequence

To run the simultaneous multinuclear MRI experiments, a modified version of the well-known gradient-echo sequence was used, in which a TTL trigger signal was inserted before the RF excitation to maintain precise timing. As it is shown in Fig. 4 a triggering signal (**TTL Trig**) initiates the imaging procedure by signaling the start from the Bruker system. Then the RF excitation pulse is modified such that two slices with frequency bands significantly apart are simultaneously excited by UHFLI. Finally, the received gradient echo which is a frequency multiplexed signal from two nuclei is received by the UHFLI.

2.5. Effect of oversampling

To compare the performance of the UHFLI with the commercial system, MRI was conducted using the standard Bruker coil with a 10 mm NMR-Tube containing distilled water. Two MRI scans were performed, one utilizing UHFLI and the other using the Bruker RF transceive channel as illustrated in Fig. 5.a and Fig. 5.b, respectively. The results demonstrate identical sizes of the images, evident by the absence of both green and blue pixels in the overlaid images shown in Fig. 5.c. Additionally, Fig. 5.d highlights the region-of-interest, where SNR calculations revealed values of 53 ± 2.63 and 47.77 ± 3.87 for UHFLI

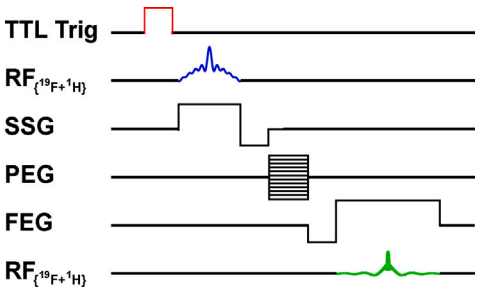

Fig. 4. A modified version of the gradient-echo pulse sequence, enabling simultaneous multinuclear MRI. The gradients are controlled and driven by the Bruker system, whereas the RF excitation and acquisition are carried out by the UHFLI. A TTL trigger from the Bruker system precedes the RF excitation to maintain time synchrony.

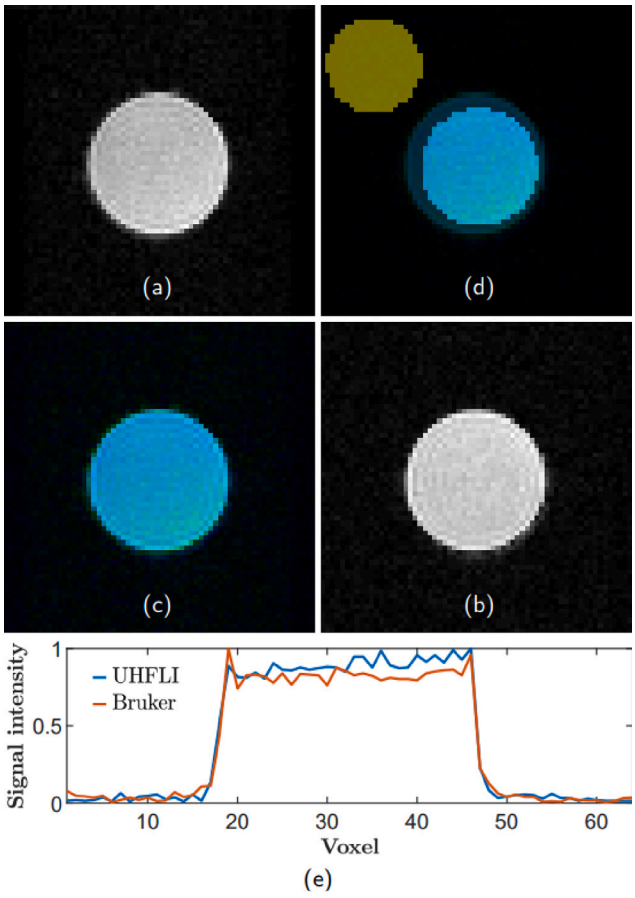

Fig. 5. (a) ^{1}H MRI of a 10 mm tube filled with distilled water acquired via the UHFLI. (b) MRI of the same sample acquired via the Bruker receiver. (c) Overlaid images ($[R, G, B] = [0, (a), (b)]$) show exact size of the two images. (d) Signal and noise regions that were chosen for SNR calculation. FOV = 20 × 20 mm^2, slice thickness = 5 mm, flip angle = 30°, image size = 64 × 64 pixels, image bandwidth = 50 kHz. (e) Center line of images (a) and (b).

and Bruker respectively, showing a slightly superior performance of the UHFLI, thanks to its robust oversampling capability. A plot of the center line for the images in (a) and (b) is shown in Fig. 5e. An additional comparison of the UHF receiver's performance with the Bruker receiver, conducted through a single-pulse NMR experiment, is presented in the supplementary material (Figure S3).

Oversampling is an interesting feature of the UHFLI enabled by its ADC's high sampling rate (1.8 GHz) and the fast processing capability of its internal field programmable gate array (FPGA) and can significantly improve the SNR. According to Richard G Lyons [19], oversampling

improves the effective number of bits of an ADC by lowering the power spectral density of its quantization noise as it is spread over a larger frequency range. The enhancement of signal-to-quantization noise due to oversampling can be calculated as:

$$\mathrm{SNR}_{\mathrm{A/D\text{-}gain}} = 10 \cdot \log_{10}\left(\frac{f_{\mathrm{OSR}}}{f_{\mathrm{Nyq}}}\right) \quad (1)$$

where f_{OSR} is the oversampling frequency and f_{Nyq} is the Nyquist sampling frequency. The signal-to-quantization noise is related to the effective number of bits (ENOB) through the following equation [20]:

$$\mathrm{SNR} = 6.02 \cdot \mathrm{ENOB} + 1.76 \quad (2)$$

Thus for an imaging bandwidth of 50 kHz with $f_{\mathrm{Nyq}} = 100$ kHz, the oversampling of the UHFLI results in an effective resolution of approximately 19 bits. According to Bruker's manual, the ADC's sampling rate is 20 MSa s^{-1}. This allows for varying oversampling ratios based on the signal bandwidth before the digital receiver unit (DRU). For example, the sharpest digital filter has a bandwidth of 1.25 MHz, resulting in an oversampling ratio of 8. This ratio provides an effective resolution of 16–20 bits depending on the signal bandwidth after digital demodulation.

The UHFLI, on the other hand, benefits from the high sampling rate of the ADC to increase its effective bit resolution beyond the 12 bits depending on the bandwidth of the desired signal and the order of the digital filters which can be up to the 8th. The digital filters of the UHFLI always keep a large enough bandwidth compared to the signal bandwidth to avoid aliasing. This allows oversampling of the demodulated signals during the transfer to the host PC, enabling thereby offline decimation to further enhance the SNR.

To explore the effect of this oversampling on the image quality, a series of MRI experiments were conducted with different oversampling factors, α. In all experiments, we used a 3rd-order digital filter of the UHFLI. To demonstrate the impact of oversampling, Fig. 6 depicts an MRI experiment conducted on a 5 mm NMR tube (Fig. 7) filled with distilled water with various oversampling factors. In Fig. 6.a$_1$, the surf level of the decimated images is observed to rise with increasing α. Subsequently, Fig. 6.a$_2$ displays the increase in SNR resulting from decimating oversampled data. The decimation is achieved by applying a 2D Fourier transform to the oversampled data. This process implicitly averages the extra samples due to the summing nature of the Fourier transform. Consequently, the resulting image has dimensions of $n \times m \cdot \alpha$. It is then resized to $n \times m$ by trimming the extensions along the frequency encoding axis, effectively performing a low-pass filtering on the image. Additionally, a comparison of MRI images captured using the UHFLI with an oversampling factor ($\alpha = 64$) and the Bruker is presented in Figs. 6.b and 6.c, with SNR values of 77 and 63, respectively. A plot of the center line for the images in (b) and (c) is depicted in Fig. 6d.

The sample holder utilized in the previous experiment, as well as all subsequent experiments in this paper, can be seen in Fig. 7. This holder was manufactured using a 3D resin printer (Phrozen) and comprised two concentric chambers in addition to bubble-trapping structures. The samples were arranged so that the inner chamber was filled with distilled water while the outer one contained C_6F_6. Due to the lack of direct access to the Bruker shimming routines, it was not possible to use the signals from both samples to define the shimming criterion. Therefore, the shimming procedure was exclusively conducted on the ^{19}F outer sample. Consequently, this action inherently resulted in the inner sample being shimmed due to its geometrical arrangement.

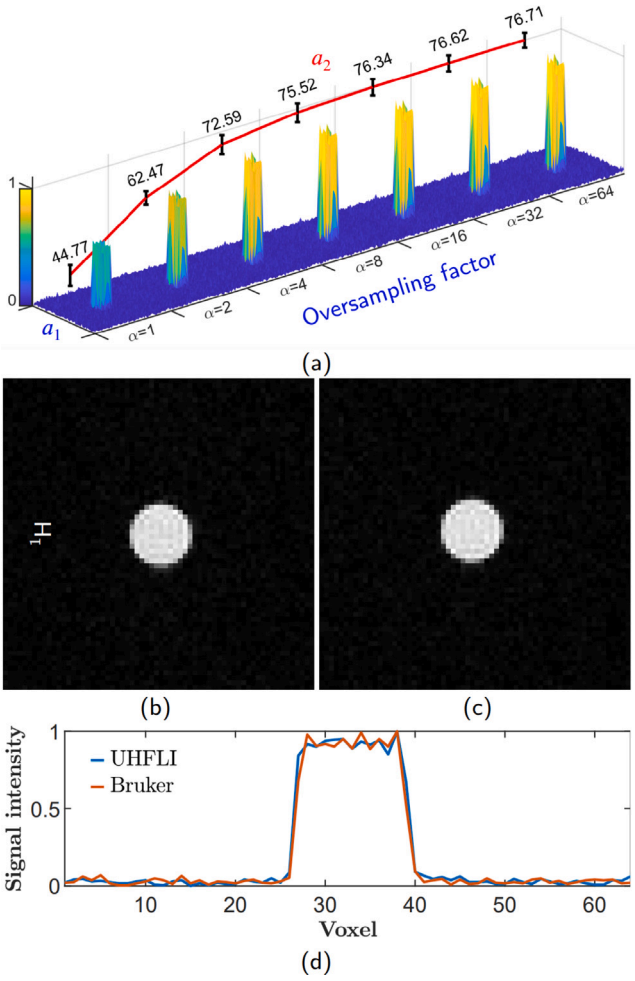

Fig. 6. (a) Effect of oversampling on SNR (image bandwidth = 50 kHz, oversampling ratio $\alpha = 2^i$, $i = \{i \mid i \in w, i = 0, \ldots, 6\}$) (b) MRI of 5 mm tube filled with water utilizing the UHFLI ($\alpha = 64$). (c) MRI of the same sample using the Bruker RF channel. FOV = 20 × 20 mm^2, slice thickness = 5 mm, image size = 64 × 64 pixels, flip angle = 60°. (d) Center line of images (b) and (c).

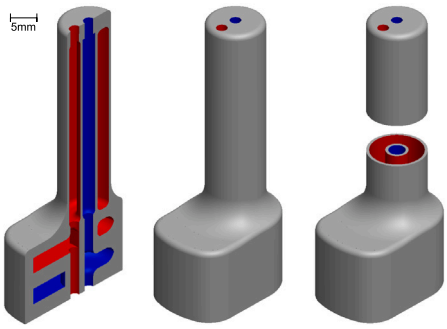

Fig. 7. CAD model of the 3D-printed sample holder, in which the blue container will contain distilled water and the red container Hexafluorobenzene (C_6F_6).

3. Results

3.1. Parallel MRI using a single receive channel

Following the experimental setup depicted in Fig. 3 and utilizing the pulse sequence of Fig. 4, Fig. 8a presents the results of a simultaneous ^{1}H and ^{19}F imaging experiment of the sample plotted in Fig. 7 using a single RF receive channel. It additionally depicts the corresponding MRI results obtained sequentially via a Bruker RF channel, Fig. 8b. A plot of the center line of the ^{1}H images is shown in Fig. 8c, whereas Fig. 8d illustrates the plot of the center line of the ^{19}F images. To ensure an accurate comparison, the amplitude of the RF pulse from both the UHFLI synthesizer as well as the Bruker RF synthesizer were gauged using an oscilloscope and were ensured to have the same amplitude before being introduced to the excitation power amplifier. The results

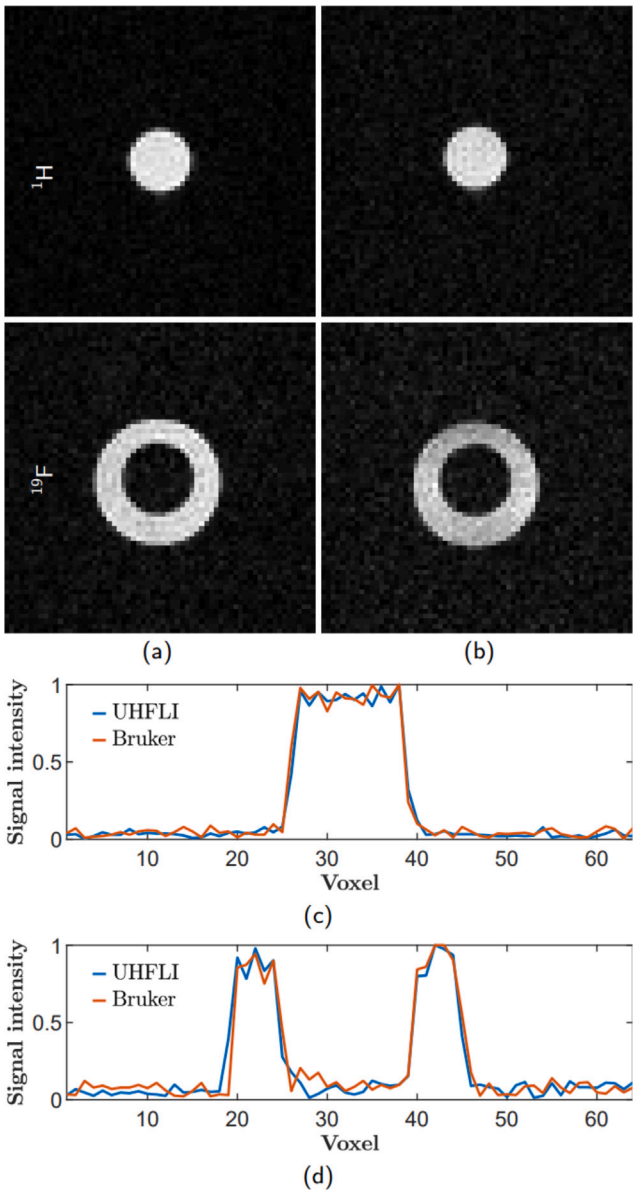

Fig. 8. (a) Simultaneously acquired MR images using the UHFLI. $SNR_{^1H} = 54.10 \pm 1.60$ and $SNR_{^{19}F} = 33 \pm 0.9$. (b) Sequentially acquired magnetic resonance images. $SNR_{^1H} = 43 \pm 1.00$ and $SNR_{^{19}F} = 29 \pm 8.9$. FOV = 20 × 20 mm^2, slice thickness = 5 mm, image size = 64 × 64 pixels, repetition time = 1 s, flip angle = 60°, image bandwidth = 50 kHz, and oversampling ratio of the UHFLI, $\alpha = 9$. (c) Center line of the ^{1}H images. (d) Center line of the ^{19}F images..

illustrated in the figure show a successful parallel acquisition of the MRI signals from two nuclei with no measurable crosstalk between them and with a slightly superior SNR for the images acquired simultaneously by the UHFLI, attributed to its oversampling.

3.2. Parallel MRI using a single transceive channel

In the preceding sections, experiments were conducted using two RF output channels combined using an RF combiner to simultaneously excite the two nuclei. However, the focus in this section is to utilize only one RF output channel for the concurrent excitation of both nuclei. Consequently, the excitation pulse must, in this case, carry dual frequencies, tailored around the Larmor precession frequencies of the targeted nuclei (^{1}H and ^{19}F). Fig. 9 shows an example of such an RF pulse that can simultaneously excite two distinct slices of water and

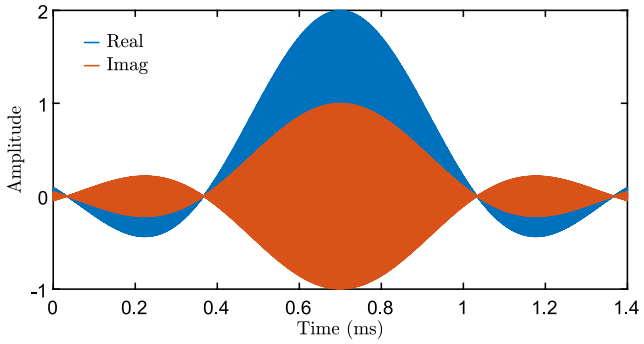

Fig. 9. A broadband slice-selective RF excitation pulse capable of simultaneously exciting ^{1}H and ^{19}F slices.

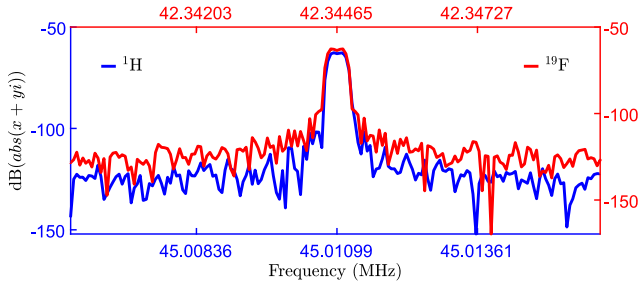

Fig. 10. Measured Fourier domain free induction decay from a signal generated by a broadband excitation pulse, for both ^{1}H and ^{19}F.

Hexafluorobenzene. The current modification involves the freeing of one RF output channel and the removal of the RF combiner, highlighted in red in the schematic of Fig. 3.

The excitation pulse depicted in Fig. 9 was designed to excite two distinct slices from the water (^{1}H) and Hexafluorobenzene (^{19}F) samples, each with a slice thickness of 5 mm, corresponding to an excitation bandwidth of approximately 3 kHz. The slices were centered at the frequencies 45.010 99 MHz and 42.344 65 MHz respectively. The pulse was calculated in Matlab by defining an ideal frequency domain profile with two rectangular pulses centered at the targeted frequencies, and then calculating their inverse Fourier transform. The carrier frequency of the UHFLI's IQ modulator was then set to the center frequency, $f_c = (45.01099 + 42.34465)/2 = 43.677\,82$ MHz. With a sequencer resolution of 4.44 ns, a waveform memory of 128 MSa, and a DAC sample rate of 1.8 GHz, the UHFLI could readily play broadband slice selective TX pulses covering almost every known nucleus, for the magnetic field strength used in this paper.

To confirm the successful implementation of the broadband selective excitation pulse, we played the pulse depicted in Fig. 9 utilizing the arbitrary waveform generator (AWG) of the UHFLI, modulating the generated wave with a 43.677 82 MHz carrier, and routed the IQ-modulated pulse to one of the RF outputs of the UHFLI. Then the generated pulse was introduced to one of the UHFLI's RF inputs which was assigned to two software IQ-demodulators with frequencies of 45.010 99 MHz and 42.344 65 MHz, respectively. The results displayed in Fig. 10 show that the resulting pulse contained two rectangular excitation profiles accurately located at the desired frequencies.

After verifying the precision of the broadband selective excitation pulse, we conducted a concurrent ^{1}H and ^{19}F MRI of the sample of Fig. 7 using a single RF transceive channel, adhering to the experimental setup of Fig. 3 while excluding the part highlighted in red. The imaging results illustrated in Fig. 11a display a faithful reconstruction of the two images with no measurable crosstalk, and with a similar SNR to the scenario where two separate RF output channels were employed. A plot of the center line of the ^{1}H and ^{19}F images is shown in Fig. 11b.

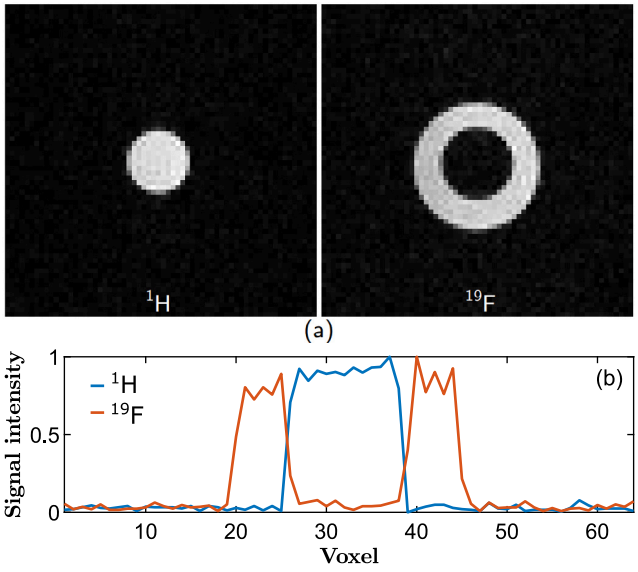

Fig. 11. (a) A parallel multinuclear MRI using a single RF transceive channel. Imaging parameters: FOV = 20 × 20 mm^2, slice thickness = 5 mm, size = 64 × 64 pixels, repetition time = 1 s, flip angle = 60°, image bandwidth = 50 kHz. SNR for ^{1}H = 62.04 ± 0.93 and for ^{19}F = 44.41 ± 2.34 (b) Center line of images in (a).

4. Discussion and outlook

In this paper, we presented a hardware-efficient approach to performing parallel multinuclear magnetic resonance imaging. The approach benefits from digital lock-in detection by digitizing a frequency multiplexed signal encompassing simultaneous MR signals from several nuclei at a very high sampling rate. The digitized signal is then applied simultaneously to multiple software-defined demodulators running at different demodulation frequencies. This allows the faithful separation and accurate reconstruction of the MR images with no measurable crosstalk. To validate this concept, a relatively broadband RF coil was built whose bandwidth was widened by purposefully lowering its Q-factor to account for the ^{1}H and ^{19}F frequencies. This concept of building broadband detectors was adopted here due to the relatively close frequencies of ^{1}H and ^{19}F. Nevertheless, if more nuclei are required, then an even more sensitive approach based on a multi-resonance configuration can be considered [21]. A resonant multinuclear coil can be constructed using either a double-resonance topology with two ports, as shown in the circuit in [22,23], or a single-port topology that incorporates inductor-capacitor (LC) traps, as illustrated in the circuits described in [24,25]. The former method necessitates an RF combiner to multiplex the signals from the two ports and connect them to the UHFLI, making the single-port approach more advantageous in this scenario. The introduced parallel muli-nuclear MRI scheme with a single RF transceive channel can acquire up to eight nuclei simultaneously with no compromise in terms of SNR or bit resolution. This number is only limited by the speed of the Field Programmable Gate Arrays (FPGA), the digital signal processing platform, of the UHFLI. Nonetheless, it is theoretically unlimited considering FPGAs with higher speeds or offline demodulation. The introduced method holds great potential for applications that necessitate the simultaneous acquisition of multi-nuclei, particularly when there is a need to have multi-dimensional monitoring of processes or reactions that are interrelated or occur simultaneously.

CRediT authorship contribution statement

Mohammad Rasool Vaezi K.: Writing – original draft, Visualization, Validation, Methodology, Formal analysis. **Jan G. Korvink:** Writing – review & editing, Supervision, Funding acquisition, Conceptualization. **Mazin Jouda:** Writing – review & editing, Supervision, Funding acquisition, Conceptualization.

Declaration of competing interest

The authors declare the following financial interests/personal relationships which may be considered as potential competing interests: Jan G. Korvink reports a relatonship with Voxalytc GmbH that includes: board membership.

Acknowledgments

This work was mainly funded by the Deutsche Forschungsgemeinschaft (DFG, German Research Foundation) - SFB 1537/1 (ECOSENSE). This work was additionally supported by the Helmholtz Association Research Area Information, Materials Systems Engineering, Topic 5 Materials Information Discovery, the SFB 1527/1 – project-ID 454252029 (HyPERiON), ERC SygG HiSCORE, and the Karlsruhe Institute of Technology. The authors additionally acknowledge support from the KIT-Publication Fund.

Appendix A. Supplementary data

Supplementary material related to this article can be found online at https://doi.org/10.1016/j.jmr.2024.107782.

Data availability

Data will be made available on request.

References

[1] Giovanni B Frisoni, Nick C Fox, Clifford R Jack Jr., Philip Scheltens, Paul M Thompson, The clinical use of structural MRI in alzheimer disease, Nat. Rev. Neurol. 6 (2) (2010) 67–77.
[2] John S Duncan, Gavin P Winston, Matthias J Koepp, Sebastien Ourselin, Brain imaging in the assessment for epilepsy surgery, The Lancet Neurol. 15 (4) (2016) 420–433.
[3] Roderic I Pettigrew, John N Oshinski, George Chatzimavroudis, W Thomas Dixon, MRI techniques for cardiovascular imaging, J. Magn. Reson. Imaging An Off. J. Int. Soc. Magn. Reson. Med. 10 (5) (1999) 590–601.
[4] Seiji Ogawa, David W Tank, Ravi Menon, Jutta M Ellermann, Seong G Kim, Helmut Merkle, Kamil Ugurbil, Intrinsic signal changes accompanying sensory stimulation: functional brain mapping with magnetic resonance imaging., Proc. Natl. Acad. Sci. 89 (13) (1992) 5951–5955.
[5] Henk Van As, Tom Scheenen, Frank J. Vergeldt, MRI of intact plants, Photosynth. Res. 102 (2009) 213–222.
[6] Igor V. Koptyug, MRI of mass transport in porous media: Drying and sorption processes, Prog. Nucl. Magn. Reson. Spectrosc. 65 (2012) 1–65.
[7] Alfredo L. Lopez Kolkovsky, Pierre G. Carlier, Benjamin Marty, Martin Meyerspeer, Interleaved and simultaneous multi-nuclear magnetic resonance in vivo. Review of principles, applications and potential, NMR Biomed. 35 (10) (2022) 1–24.
[8] Ladislav Valkovič, Marek Chmelík, Martin Kršňák, In-vivo 31P-MRS of skeletal muscle and liver: a way for non-invasive assessment of their metabolism, Anal. Biochem. 529 (2017) 193–215.
[9] Stanley J Kruger, Scott K Nagle, Marcus J Couch, Yoshiharu Ohno, Mitchell Albert, Sean B Fain, Functional imaging of the lungs with gas agents, J. Magn. Reson. Imaging 43 (2) (2016) 295–315.
[10] G Bringmann, K Wolf, M Meininger, M Rokitta, A Haase, In vivo 19 F NMR chemical-shift imaging of ancistrocladus species, Protoplasma 218 (2001) 134–143.
[11] J Keupp, PC Mazurkewitz, I Gräß lin, T Schaeffter, Simultaneous 19f and 1H imaging on a clinical 3T MR scanner, in: Proceedings of the 14th Annual Meeting of ISMRM, 848, Citeseer, 2006, p. 2847.
[12] Jochen Keupp, Jürgen Rahmer, Ingmar Grässlin, Peter C. Mazurkewitz, Tobias Schaeffter, Gregory M. Lanza, Samuel A. Wickline, Shelton D. Caruthers, Simultaneous dual-nuclei imaging for motion corrected detection and quantification of 19F imaging agents, Magn. Reson. Med. 66 (4) (2011) 1116–1122.

[13] Jeremy W. Gordon, Sean B. Fain, David J. Niles, Kai D. Ludwig, Kevin M. Johnson, Eric T. Peterson, Simultaneous imaging of 13C metabolism and 1H structure: Technical considerations and potential applications, NMR Biomed. 28 (5) (2015) 576–582.
[14] Ēriks Kupče, Kaustubh R Mote, Andrew Webb, Perunthiruthy K Madhu, Tim DW Claridge, Multiplexing experiments in NMR and multi-nuclear MRI, Prog. Nucl. Magn. Reson. Spectrosc. 124 (2021) 1–56.
[15] Ēriks Kupče, Ray Freeman, Boban K. John, Parallel acquisition of two-dimensional NMR spectra of several nuclear species, J. Am. Chem. Soc. 128 (30) (2006) 9606–9607.
[16] Eriks Kupče, Steve Cheatham, Ray Freeman, Two-dimensional spectroscopy with parallel acquisition of 1H X and 19F X correlations, Magn. Reson. Chem. 45 (5) (2007) 378–380.
[17] Mazin Jouda, Erwin Fuhrer, Pedro Silva, Jan G. Korvink, Neil MacKinnon, Automatic Adaptive Gain for Magnetic Reson. Sensitivity Enhancement, Anal. Chem. 91 (3) (2019) 2376–2383.
[18] Yen-Tse Cheng, Mazin Jouda, Jan Korvink, Sample-centred shimming enables independent parallel NMR detection, Sci. Rep. 12 (1) (2022) 14149.
[19] Richard G. Lyons, Understanding digital signal processing, 3/E, Pearson Education India, 1997.
[20] Richard Schreier, Gabor C. Temes, et al., Understanding delta-sigma data converters, vol. 74, IEEE press Piscataway, NJ, 2005.
[21] Hossein Davoodi, Mazin Jouda, Jan G. Korvink, Neil MacKinnon, Vlad Badilita, Broadband and multi-resonant sensors for NMR, Prog. Nucl. Magn. Reson. Spectrosc. 112–113 (2019) 34–54.
[22] Christopher V Grant, Siu-Ling Sit, Anna A De Angelis, Kelli S Khuong, Chin H Wu, Leigh A Plesniak, Stanley J Opella, An efficient 1H/31P double-resonance solid-state NMR probe that utilizes a scroll coil, J. Magn. Reson. 188 (2) (2007) 279–284.
[23] F. David Doty, Ruth R. Inners, Paul D. Ellis, A multinuclear double-tuned probe for applications with solids or liquids utilizing lumped tuning elements, J. Magn. Reson. 43 (3) (1981) 399–416.
[24] Siew Kan, Patrick Gonord, Single-input double-tuned mutually coupled surface coil circuits: An analysis, Rev. Sci. Instrum. 62 (10) (1991) 2427–2429.
[25] Sasidhar Tadanki, Raul D Colon, Jay Moore, Kevin W Waddell, Double tuning a single input probe for heteronuclear NMR spectroscopy at low field, J. Magn. Reson. 223 (2012) 64–67.